Three-dimensional modeling of hearing in *Delphinus delphis*

James L. Aroyan[a)]
JRJ Simulation & Design, 338 Wilkes Circle, Santa Cruz, California 95060

(Received 30 October 2000; revised 17 June 2001; accepted 3 July 2001)

Physical modeling is a fertile approach to investigating sound emission and reception (hearing) in marine mammals. A method for simulation of hearing was developed that combines three-dimensional acoustic propagation and extrapolation techniques with a novel approach to modeling the acoustic parameters of mammalian tissues. Models of the forehead and lower jaw tissues of the common dolphin, *Delphinus delphis*, were created in order to simulate the biosonar emission and hearing processes. This paper outlines the methods used in the hearing simulations and offers observations concerning the mechanisms of acoustic reception in this dolphin based on model results. These results include: (1) The left and right mandibular fat bodies were found to channel sound incident from forward directions to the left and right tympanic bulla and to create sharp maxima against the lateral surfaces of each respective bulla; (2) The soft tissues of the lower jaw improved the forward directivity of the simulated receptivity patterns; (3) A focal property of the lower-jaw pan bones appeared to contribute to the creation of distinct forward receptivity peaks for each ear; (4) The reception patterns contained features that may correspond to lateral hearing pathways. A ''fast'' lens mechanism is proposed to explain the focal contribution of the pan bones in this dolphin. Similar techniques may be used to study hearing in other marine mammals. [DOI: 10.1121/1.1401757]

PACS numbers: 43.80.Lb, 43.64.Tk, 02.70.Bf, 02.70.Pt [WA]

I. INTRODUCTION

The auditory systems of cetaceans differ significantly from those of terrestrial mammals. These differences include the absence of external pinnae, the reduction or absence of auricular cartilages and associated musculature, partial or complete occlusion of the meatal tube, a modified tympanic membrane, generally greater variation of basilar-membrane support and width within the cochlea, and increased auditory-nerve fiber diameters and ganglion cell counts (Fraser and Purves, 1960; Norris, 1968; Bullock *et al.*, 1968; McCormick *et al.*, 1970; Ridgway *et al.*, 1974; Fleischer, 1980; Ketten and Wartzok, 1990). In odontocete cetaceans (toothed whales including dolphins and porpoises), additional modifications have occurred in the tissues of the lower jaw and ear complexes that include an excavated and thinned posterior mandible, deposition of fatty tissues, and increased isolation of the tympano–periotic complex containing the middle and inner ears within an extracranial peribullar cavity (Norris, 1964, 1980; Norris and Harvey, 1974; Fleischer, 1980; Varanasi *et al.*, 1982; Morris, 1986; Ketten, 1994, 1998, 2000).

In odontocetes, it is thought that the lower jaw plays an important role in acoustic reception. Chemically distinct fats of lowered density and acoustic velocity fill the mandibular canals of odontocetes and extend back to the tympano–periotic complex.[1] Norris (1964) proposed that, among other pathways, sound may enter the head through the windows of fat that overlie the thinned pan bones of the mandible, propagate through the pan bones, and become guided or channeled back to the ear complexes by the fat bodies. Norris (1968, 1980) also speculated that the angular transmission properties of the pan bones might provide a mechanism for enhancing direction-dependent differences in the received sound field at each ear.

Several experiments with dolphins have confirmed the involvement of the lower jaw in hearing. Norris and Harvey (1974) measured a twofold increase in intensity within the lower-jaw tissues of *T. truncatus* as sound propagated from the anterior to the posterior portion of the right intramandibular fat body. Brill *et al.* (1988) found that a low acoustic attenuation hood placed over the lower jaw of an echolocating bottlenose dolphin had little impact on target discrimination performance, while a high attenuation hood resulted in a significantly lowered performance. Measurements of auditory-evoked potentials have elicited maximum responses for sources positioned over the lower jaw in dolphins (Bullock *et al.*, 1968; McCormick *et al.*, 1970). Although lower-jaw involvement in odontocete hearing now appears to be widely accepted, details of the reception pathways remain less clear. Experimental studies of sound propagation within cetacean head and ear tissues pose complex and difficult challenges for researchers attempting to clarify hearing mechanisms. Alternative approaches are therefore of interest.

The physical reception of sound at the ears of terrestrial mammals is often studied by moving an acoustic source about the head of the animal under anechoic conditions while measuring sound pressure inside the auditory meatus. Equivalent information is gained, however, by reversing the roles of source and receiver in such an experiment. The principle of acoustic reciprocity tells us that the same information would be obtained if we instead place a small source at each ear and then measure the sound field about the head. Fortunately, computers can now handle this task. Aroyan (1996) developed mammalian tissue modeling techniques

[a)]Electronic mail: jaroyan@cruzio.com

and methods for computing underwater sound fields emitted by source and tissue models. Hence, the physical reception of sound at the ears of marine mammals can be modeled.

This article describes the technique and results of simulations of sound propagation from the underwater environment to the ear complexes in the common dolphin, *Delphinus delphis*. A set of observations concerning the mechanisms of hearing in this dolphin is offered based on model results. Questions regarding propagation within the middle-and inner ears are not pursued here, although it is clear that detailed ear models could be embedded within overall head simulations of the type presented to address such questions. Single-frequency head-related transfer function (HRTF) filters for the common dolphin are derivable from the results of this study and could likewise be obtained for other marine mammals from similar studies.

II. MODEL OF THE DOLPHIN HEAD

A. Tissue density and velocity

An approximate technique was used to map the acoustic parameters of mammalian (including delphinid) soft tissues from x-ray CT attenuation data (Aroyan, 1996). This approach generates approximations of the density and velocity distributions within scanned delphinid tissues that agree well with reported measurements (Norris and Harvey, 1974). Because of its apparent simplicity, this technique may be of broad interest to researchers in tissue modeling.[2]

The base data for the current study was an x-ray CT scan of the head of a male (body length = 1.92 m) common dolphin, *Delphinus delphis* (identified as specimen D4 in Cranford *et al.*, 1996). Individual scans consisted of 320×320-pixel transverse images on a 1.5-mm square grid. The spacing between the scan planes varied from 5.0 mm over the rostrum, to 1.5 mm over the narial region, to 3.0 mm over the posterior cranium. For the hearing simulations reported here, the CT data were linearly interpolated along the body axis to planes uniformly spaced 3.0 mm apart to generate a 3.0-mm cubic grid. Figure 1(a) illustrates the skin isosurface of the interpolated tissue data (grid size 149×87×93). The current study assumed this data to be linearly related to x-ray attenuation in Hounsfield units (HU).

Tissue density was modeled using the linear mapping to image (HU) values shown in Fig. 2(a). This model is based on medical bone mineral and soft-tissue density scanning practices (Henson *et al.*, 1987; see the discussion in Aroyan, 1996). Three calibration points confirming this linear mapping were provided by the known density (0.90 g/cc) of the inner melon (Varanasi *et al.*, 1975), the known density (1.18 g/cc) of the Plexiglas specimen registration frame, and the maximum density (roughly 2.7 g/cc) of delphinid periotic bone (Lee *et al.*, 1996). Values below −138 HU were below all soft-tissue structures (except air sacs which were modeled separately). Since it was necessary to map air surrounding the scanned specimen to seawater, all points below −138 HU were mapped to the density of seawater (1.03 g/cc).

Tissue velocity information was obtained by combining the density mapping with a correlation discovered to exist between the density and velocity values reported in literature

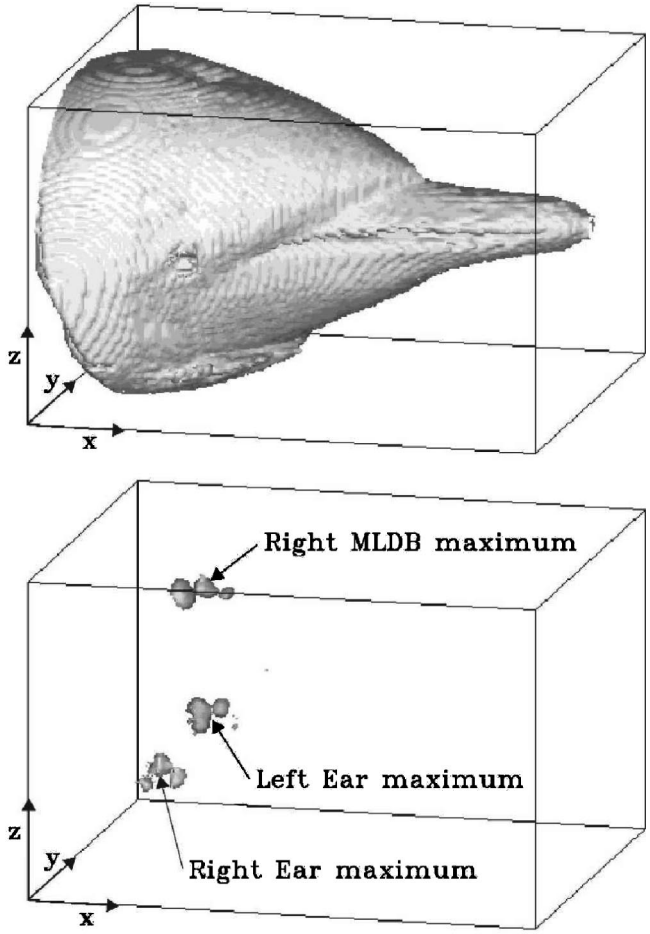

FIG. 1. (a) Visualization of the skin isosurface of the half-resolution full head model (model 3). The rectangular model volume has *x, y, z* side lengths of 44.7 cm, 26.1 cm, and 27.9 cm. (b) Illustration of an isosurface at 30% of the maximum total acoustic energy density W_{total} within the same tissue model volume (and perspective) when the model is ensonified by a 50-kHz sound beam from directly ahead. The locations of the three bright focal maxima that occur within the model are labeled.

sources for various normal fresh terrestrial mammalian soft tissues at 37 °C (Aroyan, 1996). Figure 2(b) plots density and velocity values and approximate ranges for several types of normal fresh terrestrial mammalian soft tissues and delphinid melon and lower-jaw lipids at 37 °C from literature sources (corrected for measurement temperature). The density and velocity error bars for the mammalian tissues in Fig. 2(b) correspond to 1-sigma deviations in reported values; the ranges for delphinid melon lipids correspond to the ranges reported to exist within layered melon tissues (Norris and Harvey, 1974; Varanasi *et al.*, 1975; Litchfield *et al.*, 1979). It is important to note that the velocity of fresh terrestrial mammalian soft tissues is linearly well-correlated with density in the range from normal fat to tendon. This correlation was recently confirmed to hold over the full range of human soft tissues (Mast, 2000), and has significant consequences for acoustic modeling of mammalian tissues and quantitative ultrasonic imaging.

The solid line in Fig. 2(b) indicates the mapping of soft-tissue velocity to density used in the current study. The unique delphinid melon and lower-jaw lipids were incorporated by adding an extension from normal fat down to the

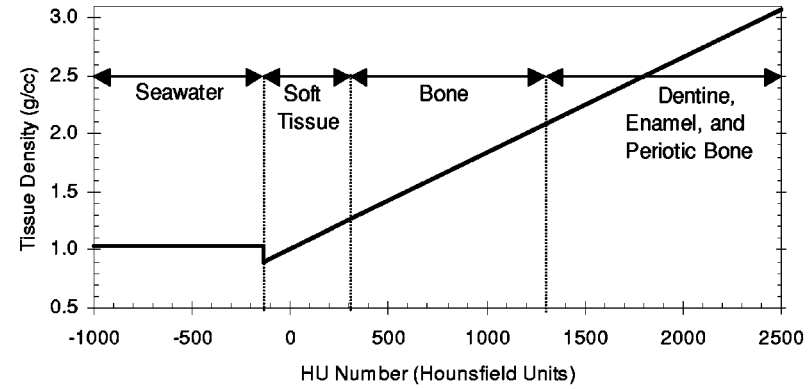

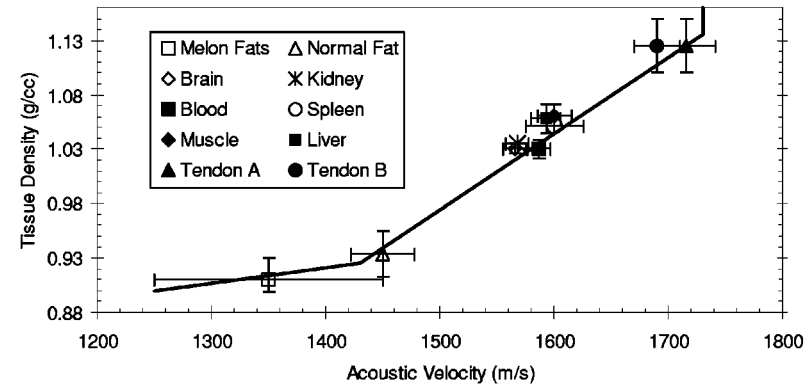

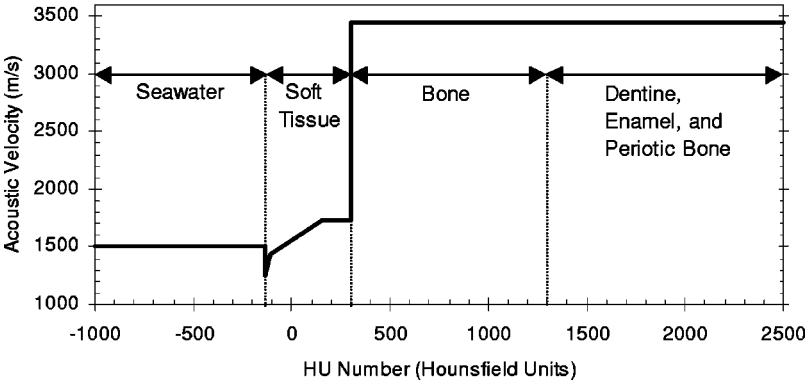

FIG. 2. (a) Plot of the linear mapping from CT values (in Hounsfield units) to tissue density used in the simulations. Tissue types corresponding to mapped CT ranges are indicated. (b) Plot of approximate values of ranges of density and velocity for several types of normal terrestrial mammalian soft tissues and delphinid melon lipids measured at 37 °C. TendonA refers to propagation perpendicular to the tendon fiber bundles. TendonB refers to propagation along the tendon fiber axis. The solid line indicates the piecewise linear mapping of density to velocity used in the simulations over the range of soft tissues. (c) Plot of the mapping from CT values (in Hounsfield units) to tissue velocity used in the simulations.

lower delphinid lipid density and velocity threshold. Given the magnitude of the variations in mammalian soft-tissue densities and velocities, a two-slope linear model was considered satisfactory for the series of simulations reported here. The acoustic phenomena of interest to this study result mainly from relatively short propagation paths (10 wavelengths or less) through fats, muscle, bone, and connective tissue of the lower head. Initial trials tested the effect of varying the piecewise-linear density-to-velocity mapping within limits of the error bars in Fig. 2(b). Because these variations did not produce significantly different emission patterns, tissue velocity was presumed to be modeled adequately by the solid line in Fig. 2(b).

Combining the linear HU-to-density mapping [Fig. 2(a)] with the empirical density-to-velocity mapping [Fig. 2(b)] determines velocity over the soft-tissue range. Figure 2(c) illustrates the HU-to-velocity mapping over the full HU scan range used in the current study. Note that the attenuation range below −138 HU (below all soft-tissue structures except air cavities) was assigned the velocity of seawater (1500 m/s), and that bone velocity for all voxels above the bone threshold at 300 HU was modeled as a constant 3450 m/s. Details of this mapping are discussed in Aroyan (1996) and Aroyan *et al.* (2000).[3]

B. Model of the ears

Definition of an appropriate model for the ears depends to some extent on assumptions regarding the function of the middle and inner ears. The densest portion of the periotic bone of each (left and right) inner ear served as the location of a small extended source (roughly 2 cc in volume) in the hearing receptivity simulations. This source location was chosen because it is assumed to be the cochlear site for each ear (Ketten and Wartzok, 1990). Such an approach assumes a picture of the hearing process in which the cochlea of the inner ears function as point receivers. It is possible that sound transduction in delphinids involves more complex

mechanisms, and alternative theories may suggest different receiver models. It should be emphasized that no attempt was made to resolve details of the propagation of sound from the surrounding bullae into the inner ears—this is clearly impossible without high-resolution ear models. Rather, the strategy adopted here was to utilize a low-resolution model of the tympanic and periotic bones with a constant velocity of 3450 m/s as an approximation for wavelengths of sound larger than the ear complexes. At 50 kHz, the wavelength of sound in bone is approximately 7 cm—roughly twice as large as the tympano–periotic complex in this dolphin. Precisely where one places the sources within the ear bones is therefore not of much consequence in the current simulations.[4]

C. Model of the air sinuses

A simple model of the peribullar cavities (surrounding much of the middle- and inner ears) and the pterygoid sinuses (extending laterally and anteriorly from the ear cavities) was used in the current study. Air sinuses were located in the *Delphinus* CT data by extracting coordinates with values below the soft-tissue threshold, and comparing the results with anatomical studies (Fraser and Purves, 1960). The full head models also included a model of the upper nasal air sacs used in the forehead emission simulations (Aroyan, 1996; Aroyan *et al.*, 2000). As in previously reported simulations (Aroyan, 1990; Aroyan *et al.*, 1992), air spaces were simulated as pressure-release surfaces by setting the pressure to zero inside the spaces. Note that this procedure eliminates any potential air–cavity resonance behavior. Although an urgently important topic for future studies, the question of whether (and under what conditions) air–cavity resonances may affect the hearing process in cetaceans is not pursued here.

III. METHODS

The following approach was used to investigate the hearing process in *D. delphis*. First, 3D acoustical models of the dolphin's head and lower jaw tissues were constructed from x-ray CT data. To provide an initial glimpse into the conduction pathways within the head, propagation of sound from forward directions into the tissue models was then simulated. Next, simulations of far-field emission patterns were conducted by placing sources at the ears in a variety of head models. By acoustic reciprocity, these emitted patterns are equivalent to the hearing receptivity patterns for those specific ear and tissue models. Hearing mechanisms were investigated by visualizing the patterns of sound propagation within the models and by examining the computed emission (receptivity) patterns.

A. Acoustic propagation method

Propagation in tissue models was simulated by numerical integration of the acoustic wave equation. In the current project, all tissues (including bone) were modeled as inhomogeneous fluids, and shear wave modes were ignored.[5] In

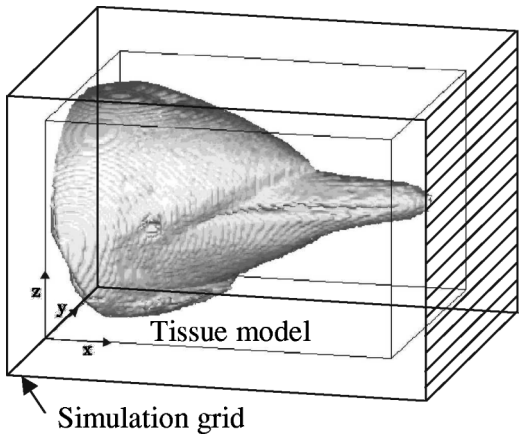

FIG. 3. Simulation grid layout. To visualize acoustic propagation patterns within the models, the front face of the grid (line filled) was used as a source to ensonify the tissue region. To simulate receptivity, the pressure and its normal derivative over a rectangular surface surrounding the ear–source and tissue models were input to an extrapolation program.

fluids of inhomogeneous density and velocity, the linearized wave equation for acoustic pressure p is (Pierce, 1981; Aroyan, 1990)

$$\frac{1}{c^2(\mathbf{x})}\frac{\partial^2 p}{\partial t^2}=\nabla^2 p-\frac{\nabla p\cdot\nabla\rho(\mathbf{x})}{\rho(\mathbf{x})}. \tag{1}$$

Both the sound speed c and density ρ are functions of position $\mathbf{x}$, while the acoustic pressure p is dependent on position and time, $p=p(\mathbf{x},t)$.

A finite-difference time-domain (FDTD) scheme was used to propagate the solution of Eq. (1) forward in time. This scheme was fourth order in the spatial derivatives of pressure, second order in the spatial derivatives of density, and second order in the time derivative of pressure (Aroyan, 1996; Aroyan *et al.*, 2000). Third-order (fourth-degree) Halpern and Trefethen absorbing boundary conditions were applied at the extreme grid edges to reduce reflections from grid boundaries (Aroyan, 1996).

Figure 3 illustrates the simulation grid layout with the tissue model region indicated. In the simulations used to visualize propagation patterns within the head and lower-jaw tissues, the front face of the grid served as a flat (cosine-windowed) source to ensonify the tissue region. In the hearing receptivity simulations, sources were placed within the models (inner ears) and emission patterns were computed as described below.

Several different quantities can be visualized to illustrate the patterns of sound propagation within tissue models. For example, one can visualize the total acoustic energy density W_{total} as the sum of the potential acoustic energy density $W_{\text{potential}}$ and the kinetic acoustic energy density W_{kinetic} (Pierce, 1981; Morse and Ingard, 1968)

$$W_{\text{total}}=W_{\text{potential}}+W_{\text{kinetic}}=\frac{1}{2\rho c^2}[\text{Re}(p)]^2+\frac{\rho}{2}|\text{Re}(\mathbf{u})|^2, \tag{2}$$

where the vector fluid velocity $\mathbf{u}=\nabla p/(i\omega\rho)$. Aroyan (1996) chose to visualize the potential energy density $W_{\text{potential}}$. In this article we visualize either the total or the potential acoustic energy density within the tissue models.

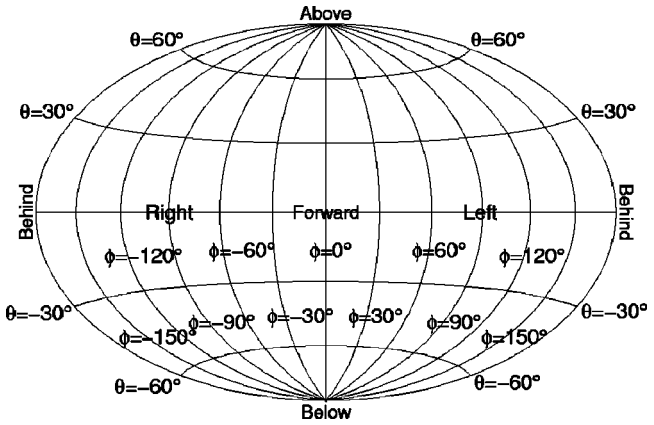

FIG. 4. Global mapping of reception direction angles θ and ϕ.

B. Acoustic extrapolation method

Computer memory limitations prohibit direct propagation of the acoustic fields emitted by the dolphin head models into the far field on 3D grids. A boundary element technique was used instead to obtain acoustic emission patterns. To compute the emission pattern of a source and tissue model, Fourier time transforms of the simulated pressure and its normal derivative over a surface immediately surrounding the tissue region of the grid were input to a far-field extrapolation routine. The transforms were interpolated with complex polynomials over boundary surface elements, allowing a high-order approximation to the extrapolation integral to be computed. The far-field surface integral and other details of this technique are provided in Aroyan (1996).

The receptivity (emission) patterns in this paper were computed for 7200 directions (3-deg increments in both latitude and longitude). The patterns are plotted using a global mapping of direction angles that is diagramed in Fig. 4. Note that vertical angle θ and horizontal angle ϕ are defined as follows: $(\theta,\phi)=(0°,0°)$ corresponds to forward of the receiver, (0°,90°) to left of the receiver, (90°,ϕ) to straight up from the receiver, etc.

IV. RESULTS OF THE SIMULATIONS

A. Visualization of focal locations within the head

To provide an overview of the acoustical properties of the head of the common dolphin, consider the result of ensonifying a full head model with a (cw) 50-kHz sound beam incident from directly forward of the animal. Figure 1(a) illustrates the skin isosurface of this full model that incorporated the skull, soft tissues, upper nasal air sacs, the peribullar cavities surrounding most of the inner ears, and the pterygoid sinuses. The full head model utilized the CT dataset mapped to a 3.0-mm cubic grid.

Figure 1(b) illustrates an isosurface at 30% of the maximum total acoustic energy density W_{total} [Eq. (2)] within the same model volume (and perspective) illustrated in Fig. 1(a). Significantly, three bright focal points occur within the model, each having a roughly funnel-shaped configuration of energy density leading up to it (more clearly visible as the isosurface level is lowered). A funnel occurs within the tissue of the forehead that narrows back to create a bright maximum just below the right monkey lips–dorsal bursae (MLDB) complex (Cranford *et al.*, 1996) within the soft tissue of the nasal complex. This clustering of focal points recurs within a small (roughly 1 cc) volume of the nasal passages over a range of ensonification directions for all frequencies tested and is quite robust with respect to tested variations of the density and velocity model mappings. Because dolphins emit biosonar pulses from their foreheads and rostrums, this focal characteristic of the upper head suggests localization of the biosonar source tissues within a small volume of the right side of the nasal passages. Further results concerning the biosonar emission system of the common dolphin are discussed in Aroyan *et al.* (2000).

Figure 1(b) also illustrates a pair of focal maxima (which narrow to point maxima as the isosurface level is increased) positioned along the anterolateral surfaces of the tympanic bulla of each respective (left and right) ear. It may be noted that the lower-jaw tissues appear to be focusing sound arriving from forward directions onto the ear complexes.

Below, we look more closely at the lower-jaw reception behavior suggested by Fig. 1(b). In order to separate out the effects of various tissue components, the results of hearing simulations using three different head models of the common dolphin will be compared. These models were constructed as follows. Model (1) included the skull, the ear bones, and a simplified upper nasal air sacs model (without peribullar cavities, without pterygoid sinuses, and without soft tissues). Model (2) included the skull, the ear bones, a simplified upper nasal air sacs model, the peribullar cavities, and the pterygoid sinuses (but *without* soft tissues or lower jaw fats). Model (3) included the complete skull, ear bones, air cavities, and soft-tissue model (with the lower-jaw fats). In all models, air spaces within the scanned tissues that were not part of the modeled air sinus and sac systems were effectively ''filled'' with seawater.

B. Visualization of propagation patterns within the lower jaw

We now examine in greater detail the lower-jaw region of the full head results. To provide visual orientation in subsequent figures, Fig. 5 provides three representations of the tissues within a lower portion of the full head model pictured in Fig. 1(a). Consider first the result of ensonifying (full) head model 2 with a 50-kHz sound beam incident from directly forward of the animal. Figures 6(a) and (b) illustrate an isosurface at 13% of the maximum potential energy density $W_{\text{potential}}$ visualized only within the lower head subvolume of Fig. 5 (viewed from the right side and from directly above). Strong reflections are seen in Fig. 6 from forward-facing portions of the rostrum and skull of model 2, with acoustic energy distributed broadly over the entire posterior and ventral skull and ear complexes. Distinct maxima do not appear near the ears.

A dramatic change occurs, however, when the soft tissues (including the lower-jaw fats) are added into the head model. Figure 7 illustrate an isosurface at 13% of the maxi-

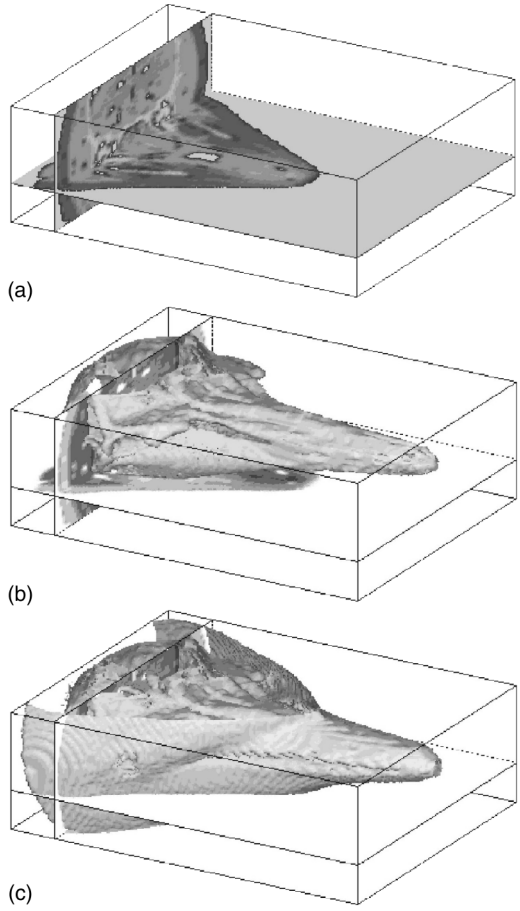

FIG. 5. (a) Tissues within the lower head subvolume illustrated by slice planes. In the horizontal slice, the lower-jaw fats are seen as slightly darker tissue surrounding the pan bones and extending back towards the middle–inner-ear complexes. Parts of the peribullar cavities can be seen around the left and right tympanic bullae (the white structures along the intersection of the two slice planes). (b) Same tissue slice planes with skull isosurface added. (c) Same tissue slice planes with skin and skull isosurfaces added.

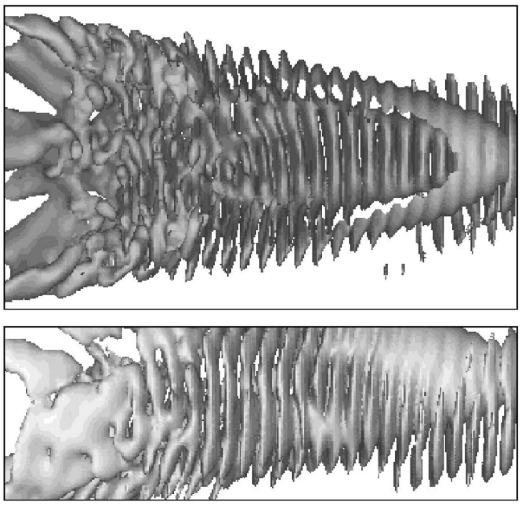

FIG. 6. Visualizations of an isosurface of acoustic energy density within the lower head tissue subvolume resulting from a 50-kHz ensonification of model #2 including the skull, the nasal air sacs, and the peribullar and pterygoid sinuses (but without soft tissue). Top diagram is a view of the lower head subvolume from above. Lower diagram is a view of the lower head subvolume from the right side.

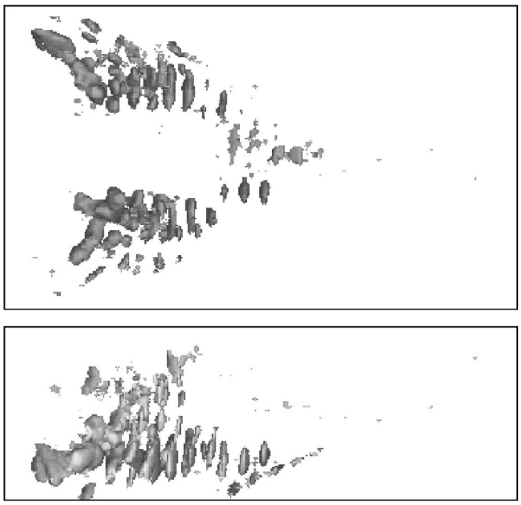

FIG. 7. Visualizations of an isosurface of acoustic energy density within the lower head tissue subvolume resulting from a 50-kHz ensonification of model #3 including the skull, the soft tissues, the nasal air sacs, and the peribullar and pterygoid sinuses. Top diagram is a view of the lower head subvolume from above. Lower diagram is a view of the lower head subvolume from the right side.

mum $W_{\text{potential}}$ visualized within the same lower head volume when model 3 was ensonified with a 50-kHz sound beam from the forward direction. The acoustic energy density now exhibits maxima immediately adjacent of both the left and right bullae [see also Fig. 1(b) at the 30% isosurface level]. Collimation or guiding appears as rough ''funnels'' of energy density passing through and below the pan bones and extending back to the region of the ear complexes. For this direction of return, the right funnel of maximum energy density touches the anterolateral region of the right tympanic bulla, while the left funnel culminates against the anterolateral region of the left tympanic bulla. Waveguiding behavior appears to be occurring within posterior portions of the intramandibular fat bodies, while both collecting and lensing appear to be occurring within anterior portions of the lateral-mandibular fat bodies. Similar maxima and focal structures were also observed in 12.5-, 25-, and 75-kHz simulations (not illustrated here). The intensification process is also evident from contours of energy density within horizontal sections of these data at the level of the ear complexes (Au *et al.*, 1998). These contours increase in roughly conical patterns that begin in the lateral-mandibular fat bodies, continue through (and below) the pan bones into the intramandibular fat bodies, and reach maximum apexes against the left and right bullae. Some incident energy also appears to be reflected laterally off of the pan bones and posterolaterally from the ear complexes themselves.

C. Individual left- and right-ear receptivity patterns

Sound propagation from far-field directions to the ears was simulated by reversing the problem and placing sources at the individual ears. The resulting far-field patterns are equivalent to the coupling between the far-field points (considered as sources) and the ear (considered as a receiver). It should be mentioned that truncation of the scanned specimen below the occipital condyle invalidates some rearward angu-

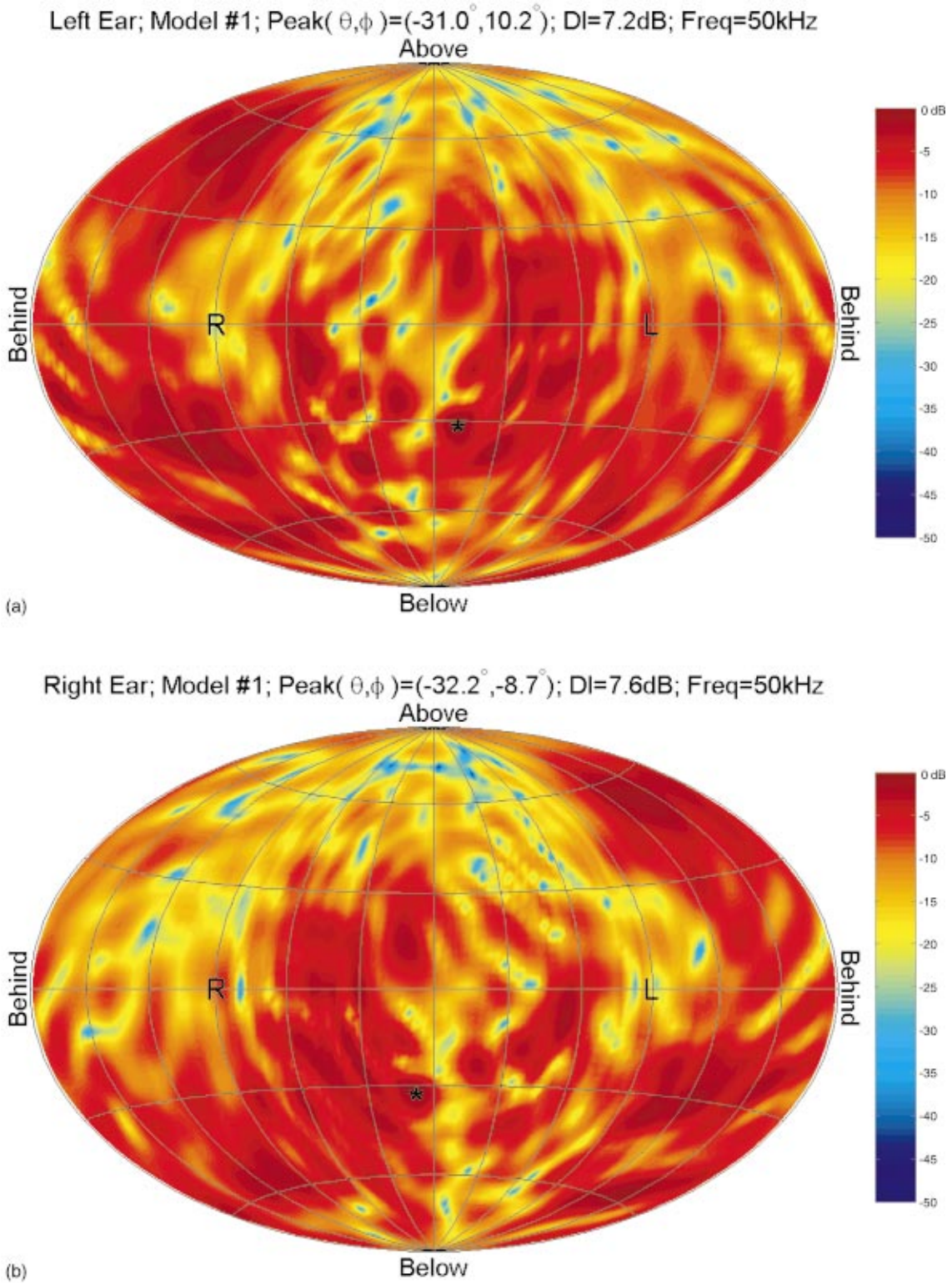

FIG. 8. Decibel maps of simulated far-field receptivity for 50-kHz sources at the inner ears of model #1 including only the skull and the nasal air sacs (without soft tissue and without the peribullar and pterygoid sinuses). (a) Source placed within LEFT inner ear. (b) Source placed within RIGHT inner ear.

lar simulation directions in head model 3 including soft tissues. The invalidated angular region for models 1 and 2 is smaller and caused only by absence of the remainder of the skeleton and air cavities posterior to the skull.

Consider first the receptivity patterns computed for head model 1. Recall that model 1 included the skull and nasal air sacs, but without soft tissues and without the peribullar cavities and pterygoid sinuses. Figure 8(a) illustrates the far-field distribution computed for a cw source of frequency 50 kHz placed within the periotic bone of the left ear. Likewise, Fig. 8(b) illustrates the far-field distribution for a 50-kHz source placed within the right ear. (Figure 4 explains the mapping of reception directions used in these plots.)

The left- and right-ear receptivity patterns in Fig. 8 have little directivity. Energy is spread over downward directions in a rather complex pattern, with an unexpected broad back-

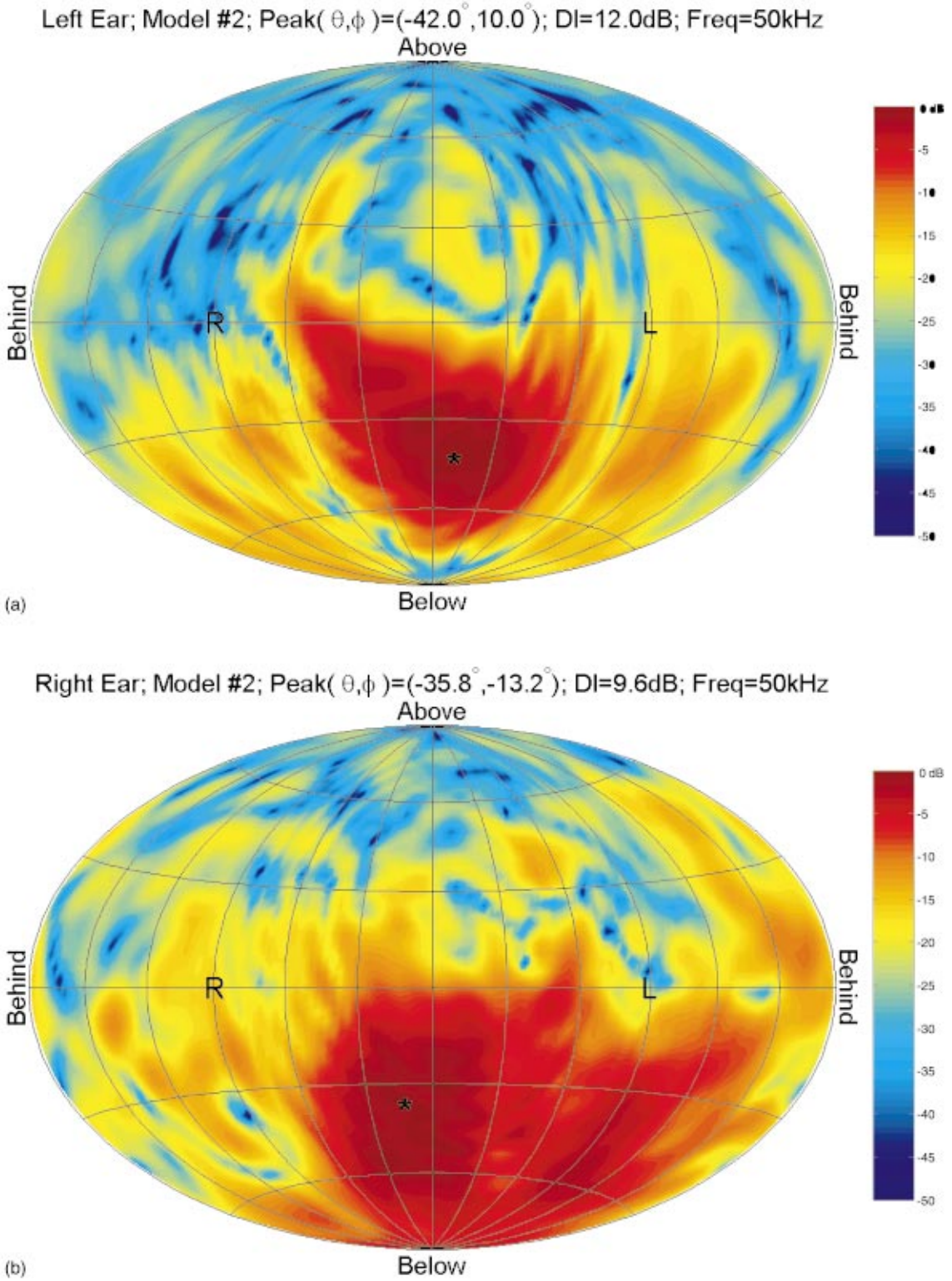

FIG. 9. Decibel maps of simulated far-field receptivity for 50-kHz sources at the inner ears of model #2 including the skull, the nasal air sacs, and the peribullar and pterygoid sinuses (but without soft tissue). (a) Source placed within LEFT inner ear. (b) Source placed within RIGHT inner ear.

ward and upward beam opposite the peribullar concavity of each ear. The sharp pattern peaks (indicated by asterisks) lie roughly 31° below the forward horizon, and occur on the same side as the respective ear. These individual pattern peaks appear to be caused by a previously unrecognized focal effect of sound propagating through the pan bones of the lower jaw. This focal effect will be discussed in the conclusions.

Consider next the effect of adding the peribullar cavities and pterygoid sinuses back into the model. Figure 9 illustrates the left- and right-ear receptivity patterns at 50 kHz for model 2 including the skull, nasal air sacs, peribullar cavities, and pterygoid sinuses, but still *without* soft tissues. Notable shifts have occurred in the patterns, which are now largely directed downward and forward. The peaks for the left and right ears lie quite low (42.0° and 35.8°, respec-

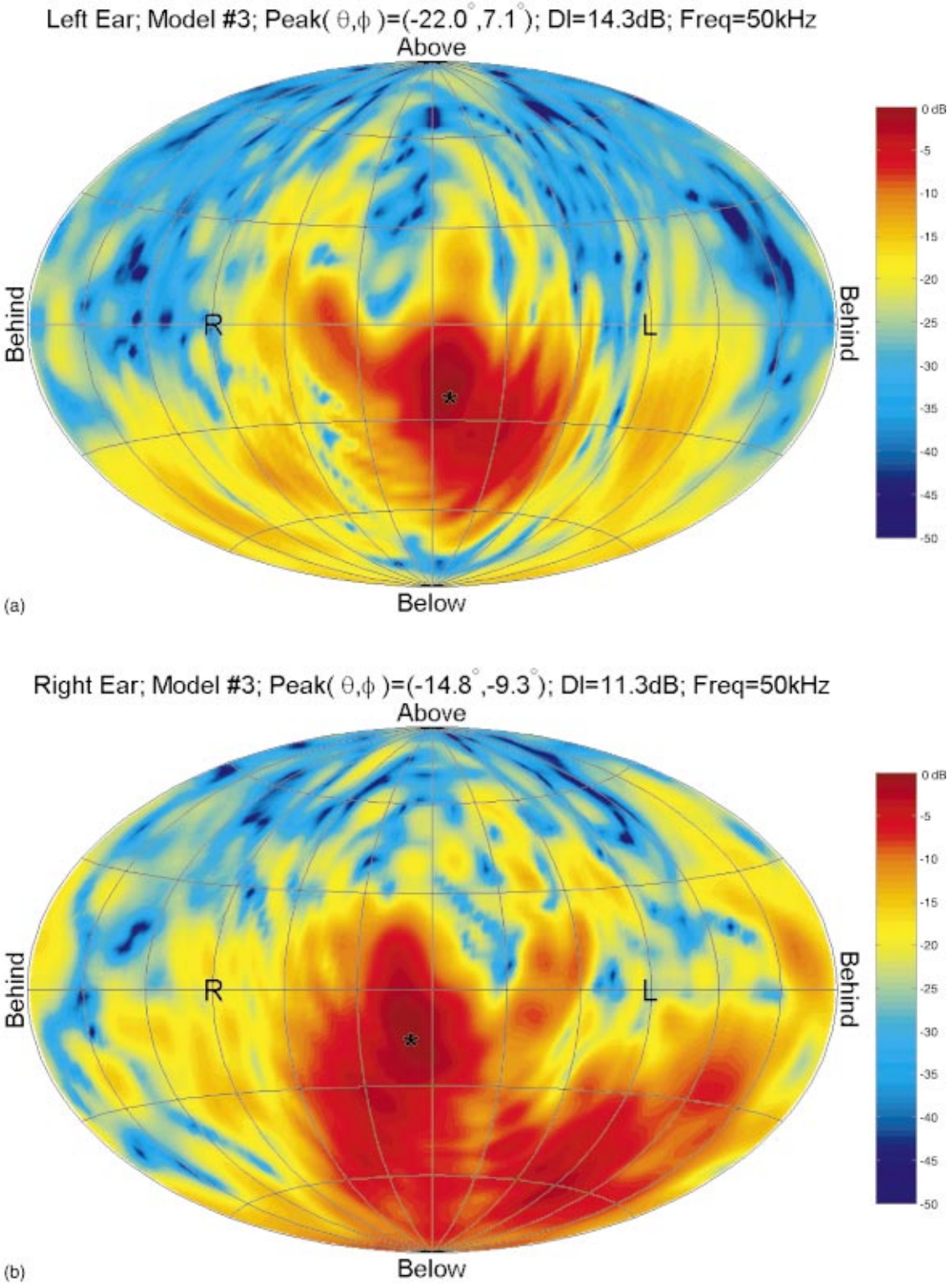

FIG. 10. Decibel maps of simulated far-field receptivity for 50-kHz sources at the inner ears of model #3 including the skull, soft tissue, nasal air sacs, and the peribullar and pterygoid sinuses. (a) Source placed within LEFT inner ear. (b) Source placed within RIGHT inner ear.

tively) below the forward horizon, and again occur on the same side as the ears themselves. In addition, several posterior and ventral lateral minor maxima may be noted.

Adding soft tissues (including the lower-jaw fat bodies) back into the model causes a further dramatic shift in the reception patterns. Figure 10 illustrates the left- and right-ear receptivity patterns at 50 kHz for model 3 containing the skull, soft tissues, nasal air sacs, peribullar and pterygoid sinuses. Note that the reception patterns have become enhanced in the forward direction, with the left- and right-ear peaks raised significantly (now 22.0° and 14.8°, respectively, below the forward horizon). This enhancement appears to be caused by the waveguiding and lensing behavior of the lower-jaw fat bundles. Note also that significant differences

in both elevation and azimuth exist between the left- and right-ear reception patterns. Again, several posterior and ventral lateral minor maxima are evident.

V. DISCUSSION OF RESULTS

The *D. delphis* hearing simulation results hold a rich set of potential implications. A series of observations based on model results is offered below. Possible refinements of the current methods as well as caveats for future applications are noted in conclusion.

As expected, a simple model of the peribullar and pterygoid sinuses was found to contribute significantly to the creation of mainly downward and forward reception patterns by insulating the ears from most other directions of incidence. Acoustic isolation of the tympano–periotic complexes from the skull is thought to be critical to maintaining interaural path differences for underwater sound localization (Dudok van Heel, 1962; Norris, 1968, 1980; Norris and Harvey, 1974; Fleischer, 1980; Oelschlager, 1986).

Directional variations were apparent in all computed receptivity patterns. Clear differences in both elevation and azimuth exist in the left versus right ear 50-kHz receptivity patterns (Fig. 10), and were also found in 12.5-, 25-, and 75-kHz patterns (not illustrated here). Most mammals utilize combinations of acoustical cues arising from intensity, phase, and frequency filtering of sound propagation to the ears to localize sound sources (Heffner and Heffner, 1992; Brown, 1994). Reception patterns that vary with horizontal and vertical angle, frequency, and distance are key to human hearing localization (Weinrich, 1984; Kuhn, 1987). Asymmetric elevation dependencies of the left- and right-ear reception patterns are known to exist in humans, cats, and barn owls (Brown, 1994). Figure 10(b) is in general agreement with the horizontal directional dependence measured experimentally by Norris and Harvey (1974) in mandibular fat near the right-ear complex of a bottlenose dolphin. Horizontal and vertical angular discrimination capabilities have been reported for the bottlenose dolphin (Renaud and Popper, 1975) and for the harbor porpoise (Popper, 1980) equal to or better than human discrimination (in air). The results of the current study suggest that both binaural (interaural intensity and phase) and monaural (frequency spectral) localization cues are available to provide horizontal and vertical directional cues to the ears of the common dolphin. Directional plots of interaural intensity and phase differences are derivable from simulated receptivity data.

Evidence was found of focal behavior resulting from sound propagation through the pan bones of the lower jaw. In order to explain this result, it is proposed that the thinner-at-the-center thickness profile (Norris, 1964, 1968) of the pan bones surrounded by low-velocity fat may act as a ''fast'' lens structure contributing to the creation of distinct forward peaks for each ear. Receptivity peaks on the same side as the ears themselves were obtained in simulated hearing patterns even for head models 1 and 2 (Figs. 8 and 9) in the absence of soft-tissue model components, showing the phenomenon to be distinct from the effect of the lower-jaw fat bodies. It is clear, however, that only an approximation to pan bone propagation can be obtained by simulation on a 3.0-mm cubic grid. As noted below, high-resolution elastic models of the mandible may be required to fully resolve acoustic propagation through the odontocete lower jaw. For this reason, the Appendix provides a supplementary analysis of the expected pan bone focal behavior for compressional waves given the pan bone geometry measured by Norris (1968). This simple analysis yields the same conclusion as the simulation result of a moderate-to-weak pan bone focal contribution to the creation of forward receptivity peaks for each ear.

The surprising differences between the acoustic energy distributions of Fig. 6 and Fig. 7 suggest that the soft tissues of the lower head markedly alter the patterns of sound propagation within the lower jaw. A dual focal structure in the lower jaw became apparent when soft tissues were added into the complete model (model #3). Sound incident below the jaw line from forward directions appears to enter the head of this dolphin in the region of the fat deposits forward of the pan bones, to propagate through (and below) the pan bones of the lower jaw, and to be guided by the left and right mandibular fat bodies back onto the left and right bullae. Isosurfaces of energy density indicate increases in acoustic intensity within the fat bodies of the lower jaw that reached maxima against the antero-lateral surfaces of the left- and right-ear complexes (Au *et al.*, 1998).

A significant fraction of the simulation energy reaching the ears in model #3, however, was found to propagate through portions of the fat bundles that extend below the mandible in *D. delphis*. This suggests that propagation along fatty pathways not passing directly through the pan bones may contribute to hearing from forward directions in this dolphin. Scans of several odontocetes reveal fats extending below the mandible and forward along each side of the lower jaw in addition to the intramandibular fats and the fats overlying the pan bones (Cranford *et al.*, 1996).[6]

The lower-jaw fats also had pronounced effects on the simulated receptivity patterns. Channeling and focusing by the lower-jaw fat bodies appear to enhance the forward receptivity of both left and right ears. Although they differ from measured response patterns, the trends in the simulation results are clear. At 12.5 kHz (results not illustrated), the left- and right-ear reception patterns were broadly distributed (average directivity index 6.2 dB), with vertical peak angles falling well below the horizon (average $-62.5°$), and horizontal peak angles well off the central axis (average 42.5° out from the same side as the respective ear). As frequency increased, the pattern peaks narrowed and rose in angle toward the forward horizon. At 75 kHz (results not illustrated), the left- and right-ear reception patterns were quite narrow (average directivity index 15.8 dB), with vertical peak angles closer to the horizon (average $-17.0°$), and horizontal peak angles approaching the central axis (average 16.2° on the same side as the respective ear). These results are consistent with the proposal that the lower-jaw fats act as forward-facing lenses and waveguides coupling a skull and air sacs (model #2) reception pattern directed more broadly downward and forward. High frequencies may be more strongly guided by the lower-jaw fats; indeed, the focal strength and steering effects of a 2D model of *D. delphis* melon tissue were found to increase with frequency (Aroyan, 1990;-

Aroyan *et al.*, 1992). The overall trend of vertical and horizontal peaks sharpening and converging into the forward direction with increasing frequency also appears consistent with the suggestion of Ketten (1998) that the anterior fat channels may be specialized for ultrasonic sonar signal conduction.

Striking differences, however, exist between the vertical peak angles of these simulated receptivity patterns and peak response angles measured for live animals. The patterns in Fig. 10 are peaked roughly 25–30° lower in vertical angle than the experimentally determined receive pattern of a bottlenose dolphin. Simulated vertical peak angles in *D. delphis* rise with frequency toward the forward horizon, but experimental response patterns for *T. truncatus* were found to be peaked between 5–10° in vertical angle for 30, 60, and 120 kHz (Au and Moore, 1984). Possible explanations for these angular discrepancies include the following:

(i) Real differences exist in the acoustic receptivity patterns of common and bottlenose dolphins.
(ii) The physical receptivity patterns of dolphins are not peaked in the forward direction for all frequencies, and auditory directional filtering is responsible for the forward response peaks measured in live bottlenose dolphins.
(iii) The inner ears may not function exclusively as point receivers as approximated by the model, and hearing response may depend in a complex fashion on sound-field distributions over the tympanic bullae or other structures.
(iv) Pan bone propagation may not be well-modeled by compressional wave algorithms.

It is appropriate here to comment only on the last of these possibilities. While the author believes the current simulations to be capable of resolving lower-jaw soft-tissue propagation up to 75 kHz (5.6 grid points per wavelength at the minimum tissue velocity), detailed studies of propagation through odontocete lower jaw bones may require high-resolution elastic modeling of the mandible.[7] Nevertheless, one might anticipate that elastic wave propagation behaviors involving shear modes are more likely to affect high-frequency results than low-frequency results—yet it is the angles of the low-frequency results that are most puzzling. The significance of the low vertical angles of the simulated reception patterns must be addressed by future research.

A final observation concerns features in the receptivity patterns that may correspond to subsidiary hearing pathways. Inferior and/or posterior lateral local maxima can be seen in Fig. 10 on the same sides as the respective ears, suggesting an increased sensitivity in lateral and inferior directions. Indeed, multiple subsidiary maxima can be identified including inferior and lateral maxima on the sides *opposite* each ear. Similar features can be identified in the receptivity patterns for model #3 at 75 kHz (not illustrated here). While these features appear to fade at 25 kHz and below (not illustrated here), the decibel differences between the sensitivity in lateral directions compared to the forward peak rapidly shrinks with decreasing frequency. Hence, even though no distinct lateral features are apparent at 12.5 kHz, the lateral sensitivity (for both ears) is only about 5 dB below the forward peak. Far-field receptivity is not equivalent to the sensitivity at the ears to sources moved over the head of a dolphin,[8] complicating comparison of simulated patterns with experimentally measured sensitivity distributions (Bullock *et al.*, 1968; McCormick *et al.*, 1970, 1980). Nevertheless, the simulation results appear in qualitative agreement with the response split reported in several studies for frequencies below 20 kHz between the sensitivity to sources at or near the external auditory meatus and sources placed over or near the mandible. This is especially true if energy loss caused by source spreading with distance from the ears is taken into account. Other features of Fig. 10 may correspond to additional pathways, including paths through melon fats of the upper head. Note, however, that soft-tissue channeling may not be the sole mechanism responsible for these subsidiary maxima. For example, lateral features are present in the receptivity patterns computed for model #2 (*without* soft tissues) at 50 kHz (Fig. 9), and are even recognizable in the patterns computed for model #1 (Fig. 8). This suggests that skull (and perhaps air sinus) reflections may be involved in creating lateral maxima. In particular, the locations of the ears within the peribullar concavities of the skull may help to create lateral and downward subsidiary maxima via reflection. It is conceivable that reflections from various skull, lower-jaw, and hyoid bone surfaces may help to provide frequency dependent directional cues, analogous to the cues created by the pinnae in humans. Clearly, further explorations are warranted.

In conclusion, the current investigation has yielded a new approach to simulation of hearing and a series of observations concerning the mechanisms of hearing in one delphinid cetacean. To the extent that the lower-jaw anatomy of the common dolphin is representative of other delphinids, it is reasonable to suggest that the lower jaws of other dolphins may also exhibit strongly directional reception. Indeed, all odontocetes may have evolved similar tissue-borne sound reception channels as an adaptation to a fully aquatic environment (Norris, 1964, 1968, 1980; Norris and Harvey, 1974; Fleischer, 1980; McCormick *et al.*, 1970, 1980; Ketten, 1994, 2000).

The core techniques used to investigate the hearing of *D. delphis* are applicable to a variety of marine mammals. Individual (or combined) right- and left-ear 3D receptivity patterns can be simulated and propagation pathways studied in other species with appropriate modifications of the methods discussed above. To this end, it is perhaps worth mentioning several potential refinements of the current methods and some caveats for future studies. Future applications could incorporate higher resolution scans,[9] scans retaining additional tissue posterior to the skull, and standard phantoms. Spiral x-ray CT techniques may be useful in resolving details of critical tissue interfaces. It should be emphasized that postmortem artifacts are always present to some extent, and careful inspection for artifacts is mandatory whenever a postmortem scan is used as the basis of living tissue models. The importance of using the freshest possible specimens and of minimizing gross-level tissue distortion is obvious. Much work remains in investigating and optimizing acoustic tissue

models based on x-ray CT data. Scanner beam energy and data postprocessing affect details of the acoustic parameter mappings. Mappings may be confirmed and/or supplemented with information from sampled measurements of tissue density and velocity. Participation by collaborating biologists in all aspects of model construction should be mandatory, and high-quality scan data should be made available to all researchers. Refined models of the peribullar and pterygoid sinuses incorporating resonances may permit exploration of mechanisms of interaction with the hearing process under varying conditions of diving and vascular infusion. A number of extensions are also possible from the standpoint of numerical propagation methods. If deemed important, tissue absorption can be incorporated into most propagation codes. Full elastic wave propagation codes are available, and may be useful for investigating thin-bone and inner-ear model propagation. Simulation of pulses rather than continuous wave propagation is also possible; in this case, k-space or pseudospectral propagation algorithms may prove optimal (Wojcik *et al.*, 1997; Mast *et al.*, 2001). Certain studies may benefit from switching to a finite-element spatial grid since it is possible to enforce grid fidelity to the geometry of critical tissue interfaces. Calculation of the acoustic intensity vector $[\mathrm{Re}(-p\mathbf{u})]$ within the tissue models may offer improved visualization of propagation pathways. It is also possible to integrate this vector over cross-sectional tissue areas to quantitatively compare the acoustic energy flux through various structures. This may, for example, be useful in quantifying degrees of waveguiding behavior. The extrapolation integral could be modified for calculation of near fields to obtain the receptivity patterns for nearby sources. As previously mentioned, simulations of the type presented in this paper can be extended to include dynamical models of the middle ears and perhaps also inner-ear models. All of the above possibilities represent exciting opportunities for future research.

ACKNOWLEDGMENTS

The author is indebted to the reviewers of this article, to Joel Kent (Elo TouchSystems, Inc., Fremont, CA), and to Darlene Ketten (Woods Hole Oceanographic Institution) for many insightful comments and suggestions. Thanks are due Ted Cranford for lending the author his CT dataset of a common dolphin, and for allowing visualization of these data in the author's dissertation and two resulting articles. Finally, the current study could not have been completed without the indirect but essential encouragement of Ken Norris (1924–1998). As one might guess, Ken was delighted with the results of this study: ''The jaw stuff, of course, warms my little geriatric heart.''

APPENDIX

This appendix offers an elementary analysis of the pan bone ''fast lens'' focal behavior. The pan bone ''window'' geometry is simplified in order to derive an order of magnitude estimate of focal distance based on the measurements of Norris (1968).

Consider sound propagation through a concave lens. A cylindrical pan bone geometry (oriented along the roughly cylindrical axis of the excavated posterior lower jaw) of radius r and acoustic velocity c_2 is assumed. The thickness is assumed to vary from h at the center to $h+\Delta h$ at the perimeter. Figure A1 diagrams the lens in cross section. Let the velocity of sound in the medium surrounding the lens be c_1. Concave lenses will focus if constructed of materials having sound speed higher than the surrounding medium ($c_2>c_1$). At some focal distance f from the lens, the center and edge rays may add in phase to create a focal point. Assuming lens thickness varies appropriately with radius, all on-axis rays will converge at this focal distance.

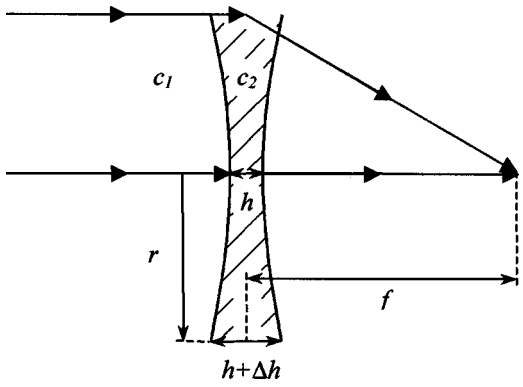

FIG. A1. Cross section of concave cylindrical lens (focusing when sound speed $c_2>c_1$).

For on-axis rays, the focal distance is easily estimated. If Δh is much smaller than radius r, the plane of the lens can be represented as a vertical line in cross section. For $\Delta h \ll r$, requiring the edge and center rays arrive at the focal distance f simultaneously leads to the following formula:

$$f=\frac{c_2^2 r^2-\Delta h^2(c_2-c_1)^2}{2\Delta h c_2(c_2-c_1)}\cong\frac{c_2 r^2}{2\Delta h(c_2-c_1)}. \tag{A1}$$

The effect of off-axis propagation on the focal length can be estimated by constructing an equivalent lens normal to the beam direction. Consider the two lenses shown in Fig. A2. These lenses will have the same focal length if the phase delay is the same for each ray. For simplicity, the case that $h=0$ is shown. Also, we assume the long focal length limit ($f\to\infty$) where beam deflection is negligible in the region of the lens. For parallel rays arriving at an angle θ with respect

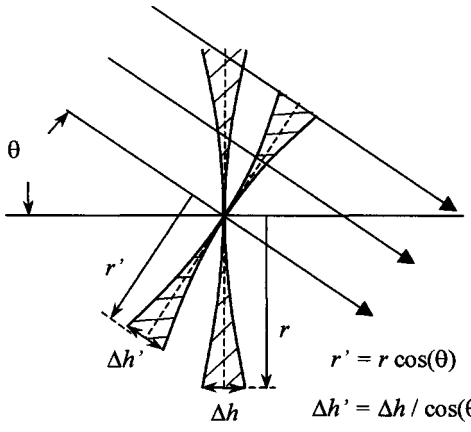

FIG. A2. Equivalent lens (in cross section) for off-axis propagation.

to the axis of the lens, the two lenses are equivalent if $r' = r\cos(\theta)$ and $\Delta h' = \Delta h/\cos(\theta)$. Because $f \propto r^2/\Delta h$, we obtain

$$f' = f\cos^2(\theta) \cong \frac{c_2 r^2 \cos^3(\theta)}{2\Delta h(c_2 - c_1)}, \tag{A2}$$

as an estimate of the modified focal length. Because f is reduced, the focusing power of the lens is increased for off-axis propagation.

Norris (1968) tabulated measurements of pan bone window dimensions and thickness variations for 11 different species of odontocetes. From these data, r is roughly estimated to vary between 2–5 cm, and Δh to be of order 1–2 mm. For compressional wave velocities c_1 and c_2, we estimate $c_1 = 1300$ m/s in the fats surrounding the pan bone, and $c_2 = 3500$ m/s in the compact homogeneous pan bone. Strictly speaking, angle θ corresponds to the angle of sound incidence on the pan bone within the surrounding fats. This angle will vary for different geometries of the water–skin–fat–bone interfaces and for different directions of reception. For sound incident from directly forward of the animal, $\theta = 28°$ is a rough estimate based on the skin surface angle information in Norris (1968) and application of Snell's law through the water–skin–fat interfaces. Because curvature is small over the central areas of the pan bones that were measured, curvature is ignored here.

The above assumptions yield estimates of f [using Eq. (A2)] that vary between 11 and 140 cm. In conjunction with soft-tissue channeling over a total propagation distance within the lower-jaw tissues of roughly 10–20 cm for sound paths passing through the pan bone in midsized delphinids, the pan bone could contribute a moderate-to-weak focusing effect.

[1]Morris (1986) provides a summary of research on the biochemical composition of these fats.

[2]Note that scanning and data treatment methods appropriate for other applications may differ from the methods used in the current investigation.

[3]Tissue absorption was deemed insignificant over the frequency range of interest to this study, and was not incorporated into the current tissue models.

[4]High-resolution middle-ear models (see, for example, Wada *et al.*, 1992) could be embedded within full head models to study detailed aspects of sound propagation within the ear complexes.

[5]Shear modes are heavily damped in soft tissues and thus are expected to have little effect on soft-tissue propagation. Acoustic propagation through the bones of the lower jaw, however, may require shear wave modes for complete solution.

[6]The morphology of these fat bodies deserves clarification along with their acoustic functionality. For example, in one species (*Kogia breviceps*), the fats lying below the lower jaw appear substantially larger in cross-sectional area than the intramandibular fats and the fats overlying the pan bones.

[7]Note, however, that the physical effect of increasing the thickness of a panel of bone-like material submerged in seawater from 1.5 to 3.0 mm lowers compressive sound power transmission at 50 kHz by less than 18 percent at normal incidence (Norris, 1968).

[8]Physical reception at the ears due to sources moved over the skin of the dolphin's head should be influenced by signal type, source directivity and distance from the ear complex, as well as the efficiency of tissue channeling. In-air measurements add the additional distortion of a highly reflective skin–air interface. The receptivity measured using this approach is not the transfer function between the skin surface and the individual ear complexes, nor is it the same thing as the far-field directional receptivity of the ears.

[9]The importance of improved resolution depends on both the properties of the tissues being modeled and the wavelengths simulated. Low-resolution models may be sufficient to model the lower frequency hearing ranges of most noncetacean marine mammal species.

Aroyan, J. L. (**1990**). "Numerical simulation of dolphin echolocation beam formation," M. S. thesis, University of California, Santa Cruz.

Aroyan, J. L. (**1996**). "Three-dimensional numerical simulation of biosonar signal emission and reception in the common dolphin," Ph.D. dissertation, University of California, Santa Cruz.

Aroyan, J. L., Cranford, T. W., Kent, J., and Norris, K. S. (**1992**). "Computer modeling of acoustic beam formation in *Delphinus delphis*," J. Acoust. Soc. Am. **92**, 2539–2545.

Aroyan, J. L., McDonald, M. A., Webb, S. C. Hildebrand, J. A., Clark, D., Laitman, J. T., and Reidenberg, J. S. (**2000**). "Acoustic Models of Sound Production and Propagation," in *Hearing by Whales and Dolphins*, edited by W. W. L Au, A. N. Popper, and R. R. Fay (Springer, New York), pp. 409–469.

Au, W. W. L., and Moore, P. W. B. (**1984**). "Receiving beam patterns and directivity indices of the Atlantic bottlenose dolphin," J. Acoust. Soc. Am. **75**, 255–262.

Au, W. W. L., Mohl, B., Nachtigall, P. E., Pawloski, J., and Aroyan, J. L. (**1998**). "Acoustic pathways of hearing in the bottlenose dolphin, *Tursiops truncatus*," J. Acoust. Soc. Am. **103**, 2908(A).

Brill, R. L., Sevenich, M. L., Sullivan, T. J., Sustman, J. D., and Witt, R. E. (**1988**). "Behavioral evidence for hearing through the lower jaw by an echolocating dolphin (*Tursiops truncatus*)," Marine Mammal Sci. **4**, 223–230.

Brown, C. H. (**1994**). "Sound Localization," in *Springer Handbook of Auditory Research: Comparative Hearing: Mammals*, edited by A. N. Popper (Springer, New York), pp. 57–96.

Bullock, T. H., Grinnell, A. D., Ikezono, E., Kameda, K., Katsuki, Y., Nomoto, M., Sato, O., Suga, N., and Yanagisawa, K. (**1968**). "Electrophysiological studies of central auditory mechanisms in cetaceans," J. Comp. Physiol. **59**, 117–156.

Cranford, T. W., Amundin, M., and Norris, K. S. (**1996**). "Functional morphology and homology in the odontocete nasal complex: Implications for sound generation," J. Morphol. **228**, 223–285.

Dudok van Heel, W. H. (**1962**). "Sound and Cetacea," Netherlands J. Sea Res. **1**, 407–507.

Fleischer, G. (**1980**). "Morphological adaptations of the sound conducting apparatus in echolocating mammals," in *Animal Sonar Systems*, edited by R. G. Busnel and J. R. Fish (Plenum, New York), pp. 895–898.

Fraser, F. C., and Purves, P. E. (**1960**). "Hearing in cetaceans: Evolution of the accessory air sacs and the structure and function of the outer and middle ear in recent cetaceans," Bull. British Mus. (Nat. Hist.), **7**, 1–140.

Heffner, R. S., and Heffner, H. E. (**1992**). "Evolution of sound localization in mammals," in *The Evolutionary Biology of Hearing*, edited by D. B. Webster, R. R. Fay, and A. N. Popper (Springer, New York), pp. 691–715.

Henson, P. W., Ackland, T., and Fox, R. A. (**1987**). "Tissue density measurement using CT scanning," Australas. Phys. Eng. Sci. Med. **10**, 162–166.

Ketten, D. R. (**1994**). "Functional analyses of whale ears: Adaptations for underwater hearing," IEEE Proc. Underwater Acoust. **1**, 264–270.

Ketten, D. R. (**1998**). "Dolphin and bat sonar: Convergence, divergence, or parallelism," 4th International Biosonar Conference 1:43.

Ketten, D. R. (**2000**). "Cetacean ears," in *Hearing by Whales and Dolphins*, edited by R. R. Fay, A. N. Popper, and W. W. L. Au (Springer, New York), pp. 43–108.

Ketten, D. R., and Wartzok, D. (**1990**). "Three-dimensional reconstructions of the dolphin ear," in *Sensory Abilities of Cetaceans: Laboratory and Field Evidence*, edited by J. A. Thomas and R. A. Kastelein (Plenum, New York), pp. 81–91.

Kuhn, G. F. (**1987**). "Physical acoustics and measurements pertaining to directional hearing," in *Directional Hearing*, edited by W. A. Yost and G. Gourevitch (Springer, New York), pp. 3–25.

Lee, S., Hanson, D. B., and Page, E. A. (**1996**). "Some acoustical properties of the otic bones of a fin whale," J. Acoust. Soc. Am. **99**, 2421–2427.

Litchfield, C., Karol, R., Mullen, M. E., Dilger, J. P., and Luthi, B. (**1979**). "Physical factors influencing refraction of the echolocative sound beam in Delphinid Cetaceans," Mar. Biol. (Berlin) **52**, 285–290.

Mast, T. D. (**2000**). "Empirical relationships between acoustic parameters in human soft tissues," ARLO **1**(2), 37–42.

Mast, T. D., Souriau, L. P., Liu, D.-L. D., Tabei, M., Nachman, A. I., and Waag, R. C. (**2001**). ''A *k*-space method for large-scale models of wave propagation in tissue,'' IEEE Trans. Ultrason. Ferroelectr. Freq. Control **48**, 341–354.

McCormick, J. G., Wever, E. G., Palin, J., and Ridgway, S. H. (**1970**). ''Sound conduction in the dolphin ear,'' J. Acoust. Soc. Am. **48**, 1418–1428.

McCormick, J. G., Wever, E. G., Ridgway, S. H., and Palin, J. (**1980**). ''Sound reception in the porpoise as it relates to echolocation,'' in *Animal Sonar Systems*, edited by R. G. Busnel and J. R. Fish (Plenum, New York), pp. 449–467.

Morris, R. (**1986**). ''The acoustic faculty of dolphins,'' in *Research on Dolphins*, edited by M. M. Bryden and R. Harrison (Clarendon, New York), pp. 369–399.

Morse, P. M., and Ingard K. U. (**1968**). *Theoretical Acoustics* (Princeton University Press, Princeton).

Norris, K. S. (**1964**). ''Some problems of echolocation in cetaceans,'' in *Marine Bio-acoustics*, edited by W. N. Tavolga (Pergamon, New York), Vol. 2, pp. 317–336.

Norris, K. S. (**1968**). ''The Evolution of Acoustic Mechanisms in Odontocete Cetaceans,'' in *Evolution and Environment*, edited by E. T. Drake (Yale University Press, New Haven), pp. 297–324.

Norris, K. S. (**1980**). ''Peripheral sound processing in odontocetes,'' in *Animal Sonar Systems*, edited by R. G. Busnel and J. R. Fish (Plenum, New York), pp. 495–509.

Norris, K. S., and Harvey, G. W. (**1974**). ''Sound transmission in the porpoise head,'' J. Acoust. Soc. Am. **56**, 659.

Oelschlager, H. A. (**1986**). ''Comparative morphology and evolution of the otic region in toothed whales (Cetacea: Mammalia),'' Am. J. Anat. **177**, 353–368.

Pierce, A. D. (**1981**). *Acoustics: An Introduction to its Physical Principles and Applications* (McGraw-Hill, New York).

Popper, A. N. (**1980**). ''Sound emission and detection by delphinids,'' in *Cetacean Behavior: Mechanisms and Functions*, edited by L. M. Herman (Wiley, New York), pp. 1–52.

Renaud, D. L., and Popper, A. N. (**1975**). ''Sound localization by the bottlenose porpoise *Tursiops truncatus*,'' J. Exp. Biol. **63**, 569–585.

Ridgway, S. H., McCormick, J. G., and Wever, E. G. (**1974**). ''Surgical approach to the dolphin's ear,'' J. Exp. Zool. **188**, 265–276.

Varanasi, U., Feldman, H. R., and Malins, D. C. (**1975**). ''Molecular basis for formation of lipid sound lens in echolocating cetaceans,'' Nature (London) **255**, 340–343.

Varanasi, U., Markey, D., and Malins, D. C. (**1982**). ''Role of isovaleroyl lipids in channeling of sound in the porpoise melon,'' Chem. Phys. Lipids **31**, 237–244.

Wada, H., Metoki, T., and Kobayashi, T. (**1992**). ''Analysis of dynamic behavior of human middle ear using a finite-element method,'' J. Acoust. Soc. Am. **92**, 3157–3168.

Weinrich, S. (**1984**). ''Sound field calculations around the human head,'' Tech. Rep. 37, The Acoustics Laboratory, Tech. Univ. of Denmark.

Wojcik, B., Fornberg, B., Waag, R. C., Carcione, L., Mould, J., Nikodym, L., and Driscoll, T. (**1997**). ''Pseudospectral methods for large-scale bioacoustic models,'' Proc. IEEE Ultrason. Symp., Vol. 2, pp. 1501–1506.